

Article

In Vitro and In Vivo Testing of Zinc as a Biodegradable Material for Stents Fabricated by Photo-Chemical Etching

Bala Subramanya Pavan Kumar Kandala ¹, Guangqi Zhang ¹, Tracy M. Hopkins ², Xiaoxian An ³, Sarah K. Pixley ² and Vesselin Shanov ^{1,4,*}

¹ Department of Mechanical and Materials Engineering, University of Cincinnati, Cincinnati, OH 45221, USA; kandalbr@mail.uc.edu (B.S.P.K.K.); zhangg5@mail.uc.edu (G.Z.)

² Department of Pharmacology and Systems Physiology, University of Cincinnati, Cincinnati, OH 45267, USA; teriannestanley@gmail.com (T.M.H.); PIXLEYSK@UCMAIL.UC.EDU (S.K.P.)

³ Department of Pharmaceutical Sciences, University of Cincinnati, Cincinnati, OH 45267, USA; anxn@mail.uc.edu

⁴ Department of Chemical and Environmental Engineering, University of Cincinnati, Cincinnati, OH 45221, USA

* Correspondence: shanovvn@ucmail.uc.edu

Received: 18 September 2019; Accepted: 22 October 2019; Published: 24 October 2019



Abstract: There is an increasing interest in biodegradable metal implants made from magnesium (Mg), iron (Fe), zinc (Zn) and their alloys because they are well tolerated *in vivo* and have mechanical properties that approach those of non-degradable metals. In particular, Zn and its alloys show the potential to be the next generation of biodegradable materials for medical implants. However, Zn has not been as well-studied as Mg, especially for stent applications. Manufacturing stents by laser cutting has become an industry standard. Nevertheless, the use of this approach with Zn faces some challenges, such as generating thermal stress, dross sticking on the device, surface oxidation, and the need for expensive thin-walled Zn tubing and post-treatment. All of these challenges motivated us to employ photo-chemical etching for fabricating different designs of Zn (99.95% pure) stents. The stents were constructed with different strut patterns, made by photo-chemical etching, and mechanically tested to evaluate radial forces. Stents with rhombus design patterns showed a promising 0.167N/mm radial force, which was comparable to Mg-based stents. *In vitro* studies were conducted with uncoated Zn stents as control and Parylene C-coated Zn stents to determine corrosion rates. The Parylene C coating reduced the corrosion rate by 50% compared to uncoated stents. *In vivo* studies were carried out by implanting photo-chemically etched, uncoated Zn stent segments subcutaneously in a C57BL/6 mice model. Histological analyses provided favorable data about the surrounding tissue status, as well as nerve and blood vessel responses near the implant, providing insights into the *in vivo* degradation of the metal struts. All of these experiments confirmed that Zn has the potential for use in biodegradable stent applications.

Keywords: Zinc; magnesium; photo-chemically etching; *in-vitro*; *in-vivo*; histology; subcutaneously; Parylene C

1. Introduction

Coronary artery diseases are the leading cause of death worldwide [1], which is a compelling reason to continue research to develop methods and techniques for treatment. Among those methods, stenting arteries for dilation has become the standard in battling coronary artery stenosis. The currently available stents are fabricated from non-degradable metals such as titanium, stainless steel, and

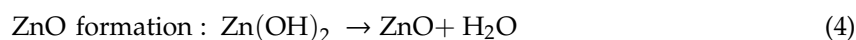
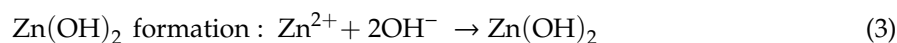
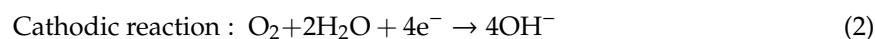
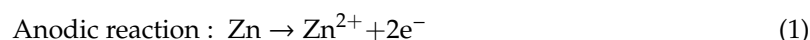
cobalt–chromium alloys. Devices made of these metals remain permanently in the body and may cause restenosis, impaired coronary vasomotion, and development of early neoatherosclerosis [2].

There is ongoing research to find biodegradable metal stents that can open obstructed arteries, keep them open for a short period of time, but then disappear after the arteries restructure because then the stents are no longer needed. The absorbable metal should be able to provide mechanical scaffolding and support and absorb in the body without harming the vessels. Typical representatives of biodegradable metals are magnesium (Mg), iron (Fe), zinc (Zn) and their alloys. Some general criteria that have proven useful for qualifying a biodegradable material as useful in stent applications are defined in Supplementary Information, Table S1 [3].

Metallic Zn appears to be one of the few physiologically acceptable metals that has not yet been actively considered for the production of bioabsorbable stents. Zn and its alloys exhibit a wide range of ultimate tensile strengths, varying from 87 to 399 MPa, and elongation to failure values from 0.9% to ~170% [4,5], so several alloys fit some of the criteria outlined in Table S1. It has been reported, in the same reference, that Zn is more ductile than Mg. Exploring the possibilities of Zn alloys with the appropriate strength, hardness, and ductility will be one of the main goals of future metallurgical engineering efforts. This would broaden the spectrum of uses for Zn and its alloys for biomedical implants. In our study, we propose a new technique, photo-chemical etching, for fabricating stents using pure Zn metal. This novel technique can be extended, in future studies, to Zn alloys that would satisfy all parameters mentioned in Table S1.

Another advantage of Zn is its corrosion characteristics. Among the three biodegradable metals, Fe has the lowest corrosion rate, which is too slow for stent applications, and its corrosion products accumulate and are difficult for the body to remove [4]. Mg has the highest corrosion rate, which could negatively affect tissues by releasing too much hydrogen and, because of this, the mechanical integrity of the stents can be compromised prior to the time needed for tissue repair. Pure Zn exhibits a high chemical activity, with an electrode potential of -0.762 V (SHE), which falls between that of magnesium at -2.372 V (SHE) and iron -0.44 V (SHE) [6,7]. Because Zn has a less negative potential compared to Mg, this reduces the chances of forming Zn^{2+} compared to the formation of Mg^{2+} . Iron has a lower negative potential compared to the other two metals, which implies that the ejection of Fe ions is more difficult. Thus, based on electrode potentials, Zn could have an optimal corrosion rate in vivo versus Fe or Mg.

The biodegradable metals are highly reactive and prone to corrosion under physiological conditions. Several degradation models have been proposed in the literature [3,8]. Generally, corrosion occurs via cathodic and anodic reactions in a near neutral (pH around 7.4) physiological environment. Metals like Mg produce oxides, hydroxides, and hydrogen gas as byproducts during their corrosion [4]. Zn also undergoes similar reaction processes, as stated below, but, unlike with Mg, this process does not produce hydrogen gas.



Under physiological conditions, where pH is controlled, electrons generated from the anodic reaction (1) would be consumed during the reduction process at the cathodic reaction (2). The other reactions (3) and (4) are likely to occur on the surface of the Zn implant. Again, note that this occurs without releasing any hydrogen gas, which is unlike Mg implants, where controlling hydrogen gas release is an important consideration [3,8,9]. Due to the presence of chloride ions in normal physiological

solutions, $\text{Zn}(\text{OH})_2$ and ZnO would aggressively react with chloride ions forming more soluble chloride salts such as $\text{Zn}(\text{OH})_2\text{-ZnCl}_2$. This process of dissolving the corrosion products $\text{Zn}(\text{OH})_2$ and ZnO exposes bare Zn metal again to physiological solutions, which promotes continuous cycles of anodic and cathodic reactions. With this progressive exposure, particles of $\text{Zn}(\text{OH})_2$ and ZnO would be separated from the Zn matrix and either precipitate or become suspended in the physiological medium [8,9].

Corrosion of Zn releases ions that are important physiologically, which offers additional support for this metal to be explored as biodegradable material for stent applications. Zn is present in all organs, tissues, fluids and body secretions, with 86% of its mass residing in skeletal muscle and bone, 6% in the skin, 5% in the liver, 1.5% in the brain, and the remaining distributed amongst the other tissues [10,11]. At the cellular level, 30–40% of the Zn existing is located in the nucleus. Zn is known as an essential element for basic metabolic processes and the recommended daily dietary intake of Zn ranges from 15 mg day⁻¹ for adult males to 2 mg day⁻¹ for infants [3,12]. Due to its physiological importance, mammals have developed sophisticated mechanisms to remove Zn from dietary constituents, absorb Zn, regulate its concentration in body fluids, transport it safely to all tissues, particularly to sites where its presence is required, and safely excrete excess amounts through the kidneys [11].

While Zn and its alloys appear to be efficacious in terms of corrosion rate and mechanical properties, major processing challenges remain before they can be manufactured into a tubular stent preform [3]. Fabricating stents by laser cutting became an industry standard, but this expensive approach introduces certain issues. Our patented alternative is based on photo-chemical etching to transfer a pattern of the stent struts onto a Mg sheet [13]. This type of Mg stent has been characterized in vitro and the results are published elsewhere [14–19]. In this study, we demonstrate that photo-chemical etching can be used to create stent materials out of pure Zn and that these materials are well tolerated by tissues in an initial *in vivo* study.

Another advantage of Zn for stent applications is that this metal, unlike Mg, is opaque to x-rays. Vascular stents are typically implanted by a catheterization procedure using x-ray fluoroscopy to guide the stent through the vasculature and position it in the target artery. Thus, the stent and/or stent deployment system must be sufficiently radiopaque (not transparent to X-rays) for visualization during fluoroscopy. Unlike Mg and its alloys, our studies demonstrated good radiopacity of the Zn stents fabricated in this work, as shown in Figure S1 (Supplementary Information).

Previous studies have demonstrated that metallic Zn shows biocompatibility when implanted in arteries in preclinical studies, greatly highlighting its promise as a base material for bioabsorbable stents [3–5,20]. One of the earliest *in vivo* studies was reported in 2013, in which pure Zn wires were implanted in the walls of the abdominal aortas of adult rats and left in for up to 6 months with no toxicity or negative tissue effects [3]. In a second study from the same lab, using the same experimental paradigm, Zn wires were left in for up to 20 months with no toxicity and the authors demonstrated a uniform corrosion rate of 0.25 mm/yr [21,22]. More recently, pure Zn stents, created by laser cutting, were inserted into the abdominal aortas of adult rabbits [9]. After 12 months, the arteries remained open, only mild inflammation was seen, and no pathology was seen in any other bodily organ. The corrosion pattern was well characterized, and some features were a loss of ~20% of the stents by 6 months and ~42% of the stents by 12 months. In addition, the corrosion products had not accumulated, showing good cellular clearance of these materials [9].

Alloys of Zn–Mg alloys are also of interest but have previously been considered primarily for orthopedic applications [23,24]. Zn–1Mg, Zn–1Ca, and Zn–1Sr alloys have corrosion rates between 0.08–0.12 mm year⁻¹ in Hank's solution [25], which are lower than most Mg alloys. For biodegradable implants, this moderate corrosion rate is critical, especially for cardiovascular stent applications. However, going forward, it will be important to control the corrosion rate of Zn alloys for use in different stent applications, for example, veins versus arteries, different sizes of blood vessels, or vessels with different blood flow rates. The corrosion rate of metal can be altered either by alloying the pure metal or by modifying the surface of the metal via coating with biocompatible polymers. The work described here first examines the suitability of using photo-chemical etching to create Zn cardiovascular stent structures,

using pure Zn, and then examines initial *in vivo* tissue compatibility studies of this Zn material. This investigation also compares the *in vitro* corrosion rate of uncoated Zn stents with that of stents coated with Parylene C. Among the many potential polymeric coatings [16,19], a chlorinated Parylene, known as Parylene C, was selected as a good candidate for improving metallic implant interactions with blood [26] and we further hypothesized that it would slow the corrosion rate of Zn, which is desired in some applications, as discussed above. It was reported by Fontaine et al. [27], that Parylene C coated stents showed very low platelet attachment when compared to uncoated tantalum stents, thus hindering thrombogenicity. Parylene C is a U.S. Food and Drug Administration (FDA)-approved biocompatible polymer. It is also a transparent, crystalline and thermoplastic substance with good elastic properties, which is an important quality that is needed when the stent expands. Parylene C is used in many technical applications because it increases the surface hydrophobicity of the coated objects. In addition, at higher blood flows, Parylene C-coated surfaces demonstrated lower rates of protein adsorption, thus suppressing clotting [26]. In addition, the relatively low permeability of Parylene C [28] suggests that a conformal coating of the polymer would slow down the corrosion of biodegradable implants by preventing contact with physiological solutions. All these potential benefits of a conformal Parylene C coating on blood-exposed medical implants led us to apply this polymer on the surface of Zn stents and to study its effect on the corrosion rate of the materials.

2. Materials and Methods

2.1. Fabrication of Cylindrical Stents by Photo-Chemical Etching

Details of our work on Mg stent fabrication using photo-chemical etching have already been published [13,14,18]. We applied this knowledge to manufacture Zn stents for the current study. The starting material was a rectangular sheet of pure Zn (99.95%) with dimensions of 200 mm × 500 mm and thickness of 250 µm, purchased from Goodfellow, Oakdale, PA. The photo-chemical etching method transfers a selected pattern of the stent onto the metal sheet, followed by chemical etching. Finally, the etched sheets with desired dimensions are rolled into cylinders and laser welded along the side seam. Figure 1 illustrates the fabrication of a stent pattern on a Zn sheet using photo-chemical etching. This approach is simple, offers high throughput and does not generate residual stress in the stent. We selected three stent designs (rhombus, U, and Omega) and fabricated stents and subjected them to mechanical strength testing before and during stent expansion. The three designs are shown in Figure 2. The dimensions of the devices were selected based on our previous experience with AZ31 Mg stents, which were tested *in vivo* in peripheral arteries in a porcine model [29].

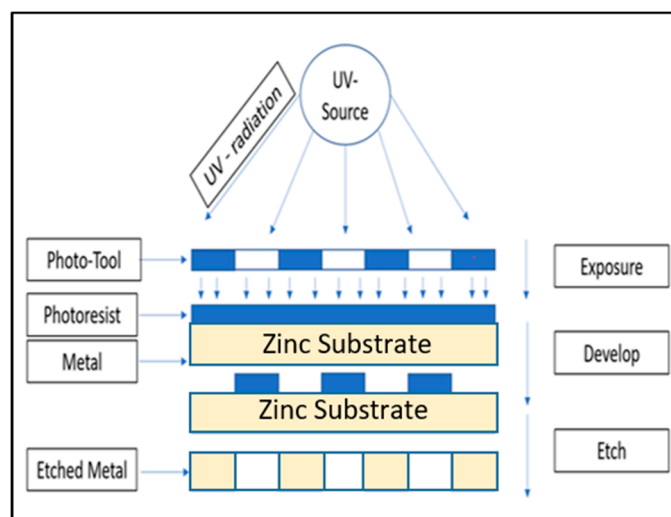


Figure 1. Illustration of the photo-chemical etching method for fabricating metal stents.

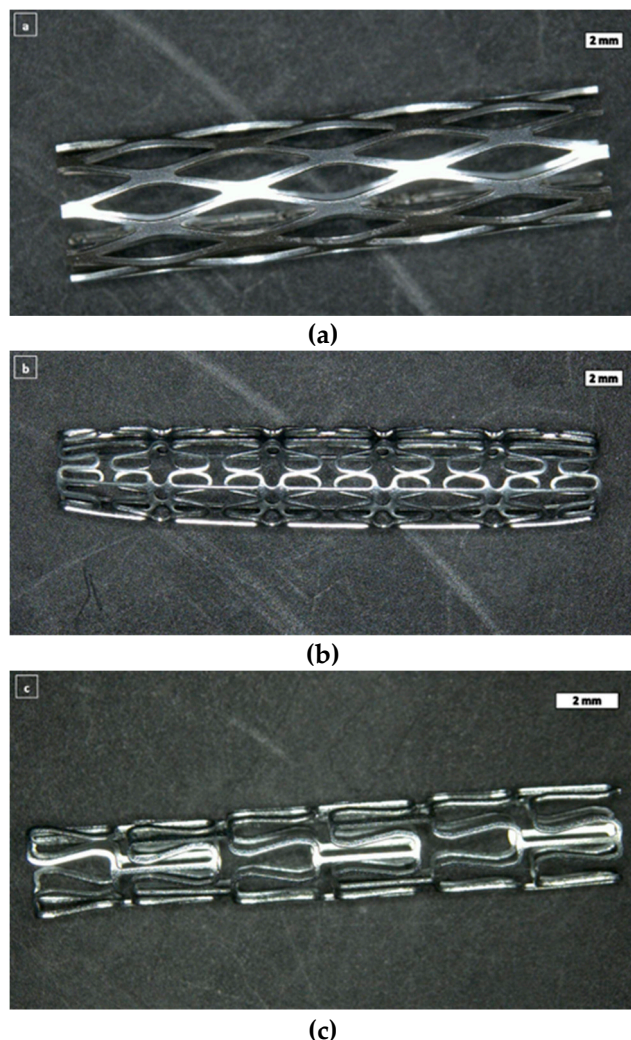


Figure 2. Pictures of Zn stents made by photo-chemical etching with different designs. (a) Rhombus design; (b) U-design; (c) Omega design.

2.2. Fabrication of Helical Stents

Numerous studies and observations have reported that blood flow through the arteries is laminar and spiral [30]. Measurement of blood velocities across the ascending aorta with a color Doppler ultrasound during coronary artery bypass surgery showed that blood appeared to “rotate in a clockwise direction” [31]. “Secondary spiral flow patterns” have been observed in the ascending aorta and at bifurcations [32], and a rotational nature to blood-flow has also been reported in the descending thoracic aorta [30]. The above-stated findings show that blood flow patterns in arteries have a spiral flow and are laminar, both of which are a result of the anatomy of smooth muscle layers and positioning of the heart. A spiral flow through the arteries preserves the blood vessels from damage by reduction of the laterally-directed forces. Bio-degradable metallic helical stents created by photo-chemical etching can potentially address these current issues, as well as meet the need for expandability and overcoming manufacturing limitations. Using photo-chemical etching, as described in Section 2.1, Zn ribbons were fabricated, as shown in Figure 3. By coiling such ribbons on a guiding rod, helical stents can be formed. No welding is required for the helical design and the dimensions of the device can be varied by the diameter of the guiding rod and the length and width of the ribbon. Details on AZ31 Mg helical stents and their unique expansion modes and corrosion behavior can be found in [13]. Ribbons manufactured in this way, of both Zn and AZ31 Mg, were used for the in vivo studies outlined below because the flat format made them preferable to complete stents for subcutaneous implantation.

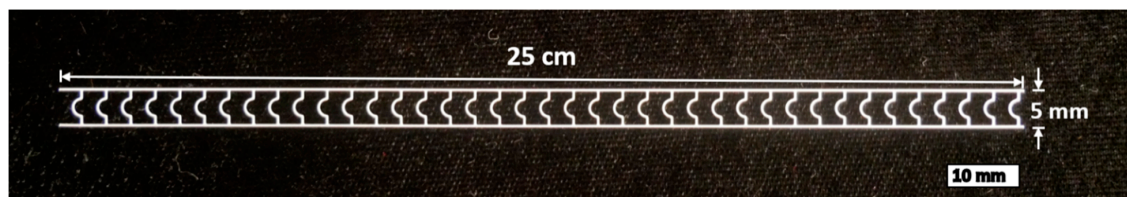


Figure 3. Picture of photochemically-etched Zn ribbon.

2.3. Mechanical Testing Setup

The radial strengths of the three stent types shown in Figure 2 were evaluated by compressing them under load after balloon expansion. The stents were expected to exhibit sufficient radial force and minimal radial recoil when deployed in animal models. In our present study, we fabricated Zn stents with the three different designs (rhombus, U, and Omega) shown in Figure 2a–c. The lengths of each unexpanded stent design were 19.5, 21 mm, and 25mm, respectively, for rhombus, U, and Omega stents. These stents were crimped onto a Percutaneous Transluminal Coronary Angioplasty (PTCA) balloon catheter delivery system. Once expanded, the radial force of each was evaluated by performing a compression test using an instrument called a UniVert (Cell Scale Biomaterial Testing, Canada) with a 10N load cell. The stents were compressed between two flat plates parallel to each other. This tool recorded the displacement and the resistive force by compressing the stent longitudinally. Resistance force generated by the stents was acquired in loading and unloading modes during the experiment.

For the compression test, stents with rhombus, Omega, and U designs were dilated with identical balloon catheters to their maximum outer diameters from the initial diameter of 4 mm each. Dilated stents were left for a few minutes to allow plastic deformation and the measured outer diameters before compression (d_i) were 7.4, 5.68, and 6.203 mm, respectively. The system's zero measurements were set to the diameter (d_i) of the stents. Step reduction was set to 0.04 mm and then the plates of the tool were allowed to reduce the gap between them, reaching a final position corresponding to 50% of the initial stent diameter (50% (d_i))). Figure 4 shows the compressive loading of a Zn stent. The resistive force exerted by the expanded stent was recorded during the loading and unloading cycles of the experiment. A hysteresis curve was obtained illustrating the crush resistance of the pure Zn stents. The resistive force was calculated using the formula below.

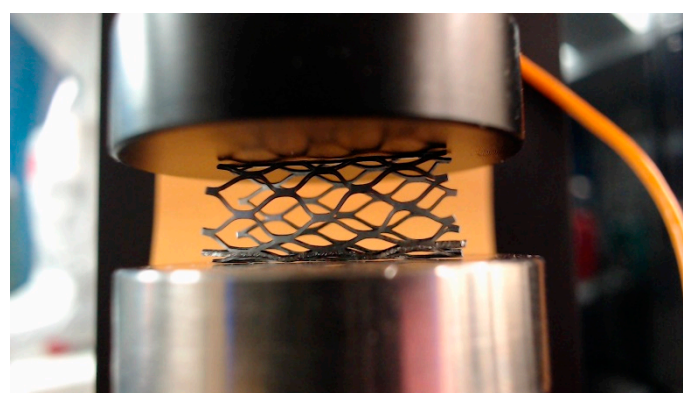


Figure 4. Mechanical/crash test of photo-chemically etched cylindrical rhombus stents.

$$\text{Radial force } \left(\frac{\text{N}}{\text{mm}} \right) = \frac{\text{The maximum resistive force exerted (N)}}{\text{The total length of the stent (mm)}}$$

2.4. Coating of the Cylindrical Stents with Paralyene C

Zn stents of the rhombus design were coated with the polymer, Parylene C, in a conformal coating process that covered all the contours of the stent topology. It was carried out by sublimation in a

Physical Vapor Deposition (PVD) chamber manufactured by Specialty Coating Systems (SCS Labcoater PDS2010, Indianapolis, IN). The sublimation process resulted in the formation of an activated polymeric Parylene C inside the deposition chamber; the chemical process of sublimation is illustrated in Figure 5. The preliminary step before coating the stents with Parylene C involved treatment with a silane primer solution, which served as a coupling agent. The hydroxyl groups from the silane primer solution interact with the metal surface and enhance the attachment of the Parylene C. This combination of primer and Parylene C has been reported previously to give good adhesion of the polymer coating, along with mechanical and chemical robustness [33,34]. The silane primer solution was prepared by mixing 1% adhesion promoter A-174 (methacryloxypropyl trimethoxysilane, Sigma-Aldrich, St. Louis, MO, USA) with 50 v % isopropyl alcohol/distilled water mixture. The primer solution was continuously stirred for 4–6 h at room temperature. Then, the Zn stents were immersed in the solution for 10 min, blow-dried and left for 20 min, followed by cleaning with 100% isopropyl alcohol in a sonication bath for a minute and subsequently blow-dried. The samples treated with the primer were transferred directly into the deposition chamber, as shown in Figure 6.

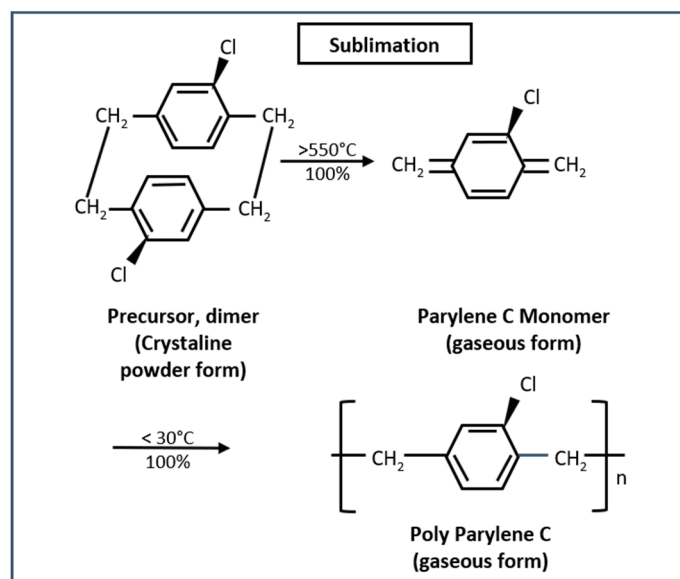


Figure 5. Parylene C sublimation process.

In this work, we used a dimer Parylene C (dichloride-1,4-xylylene—“diX-C”, Sigma-Aldrich), which is a crystalline powdered material. The initial quantity was measured by a high-precision balance and transferred into the vaporization chamber, as displayed in Figure 6. Then, Parylene C was heated to approximately 140–160 °C to initiate the sublimation process inside the vaporization chamber shown in Figure 7. The vaporized dimer of the polymer was transported to the pyrolysis chamber and heated at 670 °C, where it dissociated into two reactive monomer species. Finally, the monomers were directed to the evacuated deposition chamber, where the stents were located and maintained at near ambient room temperature. In this environment, the monomer vapor polymerized on the entire stent surface, coating it with a thin, uniform, and conformal layer of Parylene C. The process pressure in the PDS 2010 coater was set below 19 Pa. In order to evaluate the thickness of the polymer film, a flat silicon wafer partially masked with Kapton tape was placed next to the stents. After completing the Parylene C coating procedure, the Kapton tape was removed and a profilometer was used to measure the deposited film thickness. The thickness of the Parylene C can be varied by changing the initial amount of the crystalline powder dimer used, the process pressure and the evaporation temperature. The obtained conformal Parylene C coating was studied by Fourier Transform Infrared Spectroscopy (FTIR Nicolet 6700 instrument), Raman spectroscopy (Renishaw inVia instrument, with 514 nm Ar-ion laser and a

laser spot of $\sim 1 \mu\text{m}^2$), Scanning Electron Microscopy (FEI SCIOS dual beam, 5Kv, 10KV), Atomic Force Microscopy (Veeco Dimension 3100), and Contact Angle measurements (Kruss, Drop Shape Analyzer).

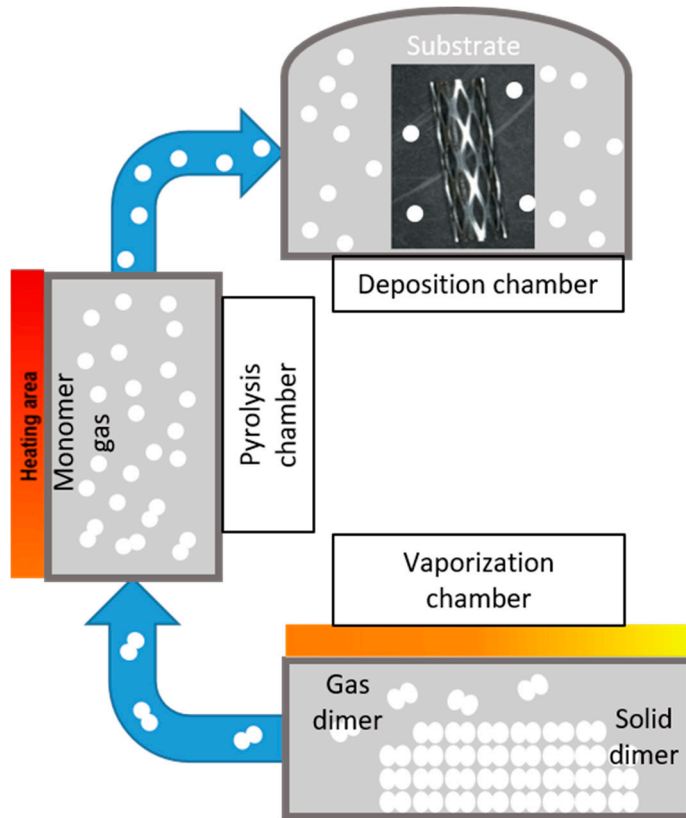


Figure 6. Illustration of the Parylene C coating procedure in a PVD.

2.5. In-Vitro Study of Surface-Modified Cylindrical Stents

2.5.1. Corrosion Rate Evaluation by Weight Loss

The corrosion rate of the Zn stents was studied by determining the weight loss of the samples in a culture medium composed of Dulbecco's Modified Eagle's Medium (DMEM) with 10% FBS (fetal bovine serum [35]) and 1% antibiotics (10,000 units/mL penicillin and 10,000 $\mu\text{g}/\text{mL}$ streptomycin). This medium has electrolytic components that mimic blood and extracellular fluids. The samples were divided into four groups: (i) uncoated and unexpanded Zn stents, (ii) uncoated and expanded Zn stents, (iii) Parylene C-coated and unexpanded Zn stents, and (iv) Parylene C coated and expanded Zn stents. The initial weight (m_i) of the test samples was recorded using a high precision ($>= 0.0001 \text{ mg}$) Sartorius weight balance. A stent surface area to culture medium volume ratio of $6 \text{ cm}^2/\text{mL}$ is outlined in ISO:10993-12 [36] for the biological evaluation of medical devices. However, with biodegradable metals, these standards are not easily applied, because the degradation products alter the medium. While a volume of $\sim 5 \text{ mls}$ would have met the ISO standard, this resulted in an undesirable change in pH, which would both modify the medium and alter corrosion. After testing, we chose a volume of 10 mL, which did not result in a pH change. So, the Zn stent samples were placed in 10 mL of the DMEM medium and left in a cell culture environment for 72 h (37°C , 100% humidity and 5% CO_2). After immersion, the Zn stents were removed and dried at room temperature. For the characterization of the corrosion products after 72 h of immersion in corrosion solution, the stents were removed from the medium and surface morphology and chemistry were analyzed using Scanning Electron Microscope (5Kv, 10KV) and Energy Dispersive Spectroscopy (EDS). Then, any corrosion products were removed through the chemical-cleaning procedure described in ISO:8407-2009 [36], which is used for the corrosion of metals and alloys. According to this standard, the test specimens were immersed in

a solution of 100 g/L ammonium chloride (NH_4Cl) in distilled water for 5 min at a temperature of 70 °C, then rinsed with 100% ethanol followed by blow-drying. The final weight (m_o) of the tested stents was recorded, and the weight loss for each sample (w) was determined using the simple equation $w = m_i - m_o$. Then, the corrosion rate C_r of the Zn stents was calculated according to the Standard Practice for Laboratory Immersion Corrosion Testing of Metals ASTM G31-72, using the equation given below [37–39].

$$C_r = \frac{w \times K}{T \times S \times \rho}$$

where C_r is the corrosion rate (mm/year), the constant K is $8.76e^4$, w is the weight loss (g), S is the sample area (cm^2) exposed to the DMEM medium, T is the time of exposure (hours), and ρ is the density of the material (g/cm^{-3}). An average and standard deviation of three measurements were determined for all four groups, as stated above.

2.5.2. Corrosion Rate Evaluation by Inductively Coupled Plasma-Mass Spectrometry (ICP-MS).

An ICP-MS apparatus (Agilent ICP-MS 7700x) was used to determine the concentration of Zn^{2+} in the culture medium before and after 72 h of in vitro immersion (2.6.2). Standard samples with different concentrations of Zn^{2+} were prepared by diluting in nitric acid to establish a calibration curve. The culture medium collected after 72 h of immersion, containing different corrosion products along with Zn^{2+} , was diluted 1000 times with nitric acid and analyzed to find the amount of Zn that dissolved during the immersion test.

2.6. In-Vivo Study

Preliminary in vivo tissue compatibility tests of Zn ribbons, with similar AZ31 magnesium samples for comparison, were conducted by subcutaneous implantation in mice. A total of eight female, 17–20 g, C57BK/6J mice were used and all procedures were approved by the University of Cincinnati Institutional Animal Care and Use Committee and followed the US National Institutes of Health guidelines for animal use. For this test, mice were anesthetized with isoflurane, given analgesics and two incisions were made on the back, just below the scapula, and two pockets were made on either side of the backbone. Inside each pocket was placed a two-strut segment (~5 mm long) of photo-chemically etched ribbon made of uncoated Zn (four mice) or uncoated Mg (AZ31 Mg, same pattern, four different mice), as shown in Figure 7. The incisions were closed with metal staples. One mouse with Zn ribbon died within 24 h of surgery for reasons not attributed to the Zn material. No issues with wound healing or animal behavior were observed in the remaining animals. After 15 days in vivo, the mice were euthanized and the skin with the attached ribbon was removed. The skin segments were fixed (4% paraformaldehyde in phosphate-buffered saline (PBS), pH 7.2) for 48 h at room temperature and rinsed in PBS. Some tissues were processed and embedded in paraffin (via standard methods) and sectioned (8- μm thick) onto slides for hematoxylin and eosin (H&E) staining (where cell nuclei are stained blue and all other cellular material is pink) or immunostaining. The Mg samples were cut with standard high-profile disposable microtome blades, but the Zn samples were cut with diamond disposable blades (both from C.L. Sturkey, Inc., Lebanon, PA). Despite the use of diamond blades, the Zn metal did cause some tissue tearing during sectioning. For tissue section immunostaining, the method was as previously described [40]. The antibodies used were specific for axons (rabbit antibody against the 200MW neurofilament protein (NF), 1/500, Sigma-Aldrich) or blood vessels (monoclonal mouse antibodies against smooth muscle actin (SMA), 1/500, Thermo Fisher Scientific, Florence, KY). Secondary antibodies were Alexa Fluor 488 conjugated goat anti-rabbit and Alexa Fluor 594 conjugated goat anti-mouse (each at 1/500). DAPI (4',6-diamidino-2-phenylindole, 1/1000, Sigma-Aldrich) was added to the secondary antibody for nuclear staining.

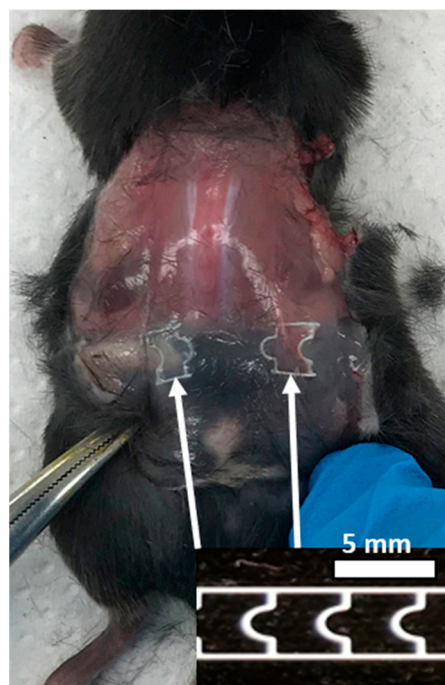


Figure 7. Segments of ribbons made of photo-chemically etched, uncoated Zn (shown) or AZ31 Mg were implanted subcutaneously in mice. The insert shows the original ribbon.

For whole tissue studies, the techniques were modified from published reports [41,42]. Skin samples with metal ribbon material were rinsed after fixation (PBS) and dehydrated in a series of increasing concentrations of methanol to 100% methanol (15–30 min incubations). Autofluorescence was quenched with Dent's bleach (methanol, DMSO and H₂O₂ in ratios 4:1:1, for 2 h) then rehydrated in steps from 100% methanol to PBS, as for dehydration. Tissue was blocked for 8 h in Tris-buffered saline (0.1M Tris with 0.15M NaCl, TBS) containing 0.5% Perkin Elmer TSA blocking reagent (Thermo Fisher). The primary antibody was added and incubated for 24–72 h on a shaker. Following five 1-h washes with PBS, the secondary antibody was added at 1/500 and incubated for 24–48 h, rinsed again, and then dehydrated with increasing amounts of methanol. Tissues were then equilibrated with the clearing agent: 1:1 benzyl alcohol: benzyl benzoate, overnight, with another change the next day, which rendered the tissues transparent. Unless otherwise specified, all materials were from Thermo Fisher Scientific.

Photography of the whole animal was done using a cell phone camera, while images of tissue sections were taken with either a Zeiss AxioCam digital camera (color) or with a QICam CCD camera (QImaging, Canada) (black and white), both on a Zeiss Axioplan imaging 2e fluorescence microscope. Fluorescent images taken with the QICam camera were pseudocolored and combined using Photoshop. Confocal images were taken on a Nikon A1R plus confocal on an upright FN1 microscope. Images were acquired with either a 4X NA 0.2 plan apochromatic or 16X NA 0.8 LWD water immersion apochromatic objective.

3. Results and Discussion

3.1. Mechanical Testing

The maximum radial force of a stent depends on its design and the material used for its fabrication. Omega, U, and rhombus design Zn stents fabricated in this work were tested under compression. Resistance force generated by the stent was recorded in loading and unloading mode, as illustrated in Figure 8. A maximum value of 0.167 N/mm radial force (force over stent length) was calculated for the stent with rhombus design, which appeared in the middle compared to the other two designs. The other two stents showed either a higher radial force 0.25 N/mm (U-design) or a very high percentage strain and

low radial force of 0.07N/mm (Omega-design). Zn stents fall in a similar radial force range compared to AZ31 Mg stents (0.1–0.25 N/mm), fabricated by photo-chemical etching and with the same design patterns as with the Zn stents. Zn stents had lower values for this parameter compared to conventional stainless-steel stents, which had a radial force of 0.4N/mm, as calculated using the data in reference [43]. However, the radial force also depends on the stent design and nature of the metal or alloy. Stents with very high radial forces require higher pressure for balloon deployment at the selected vessel location, which may eventually cause injury and, later on, more pronounced intimal proliferation [43].

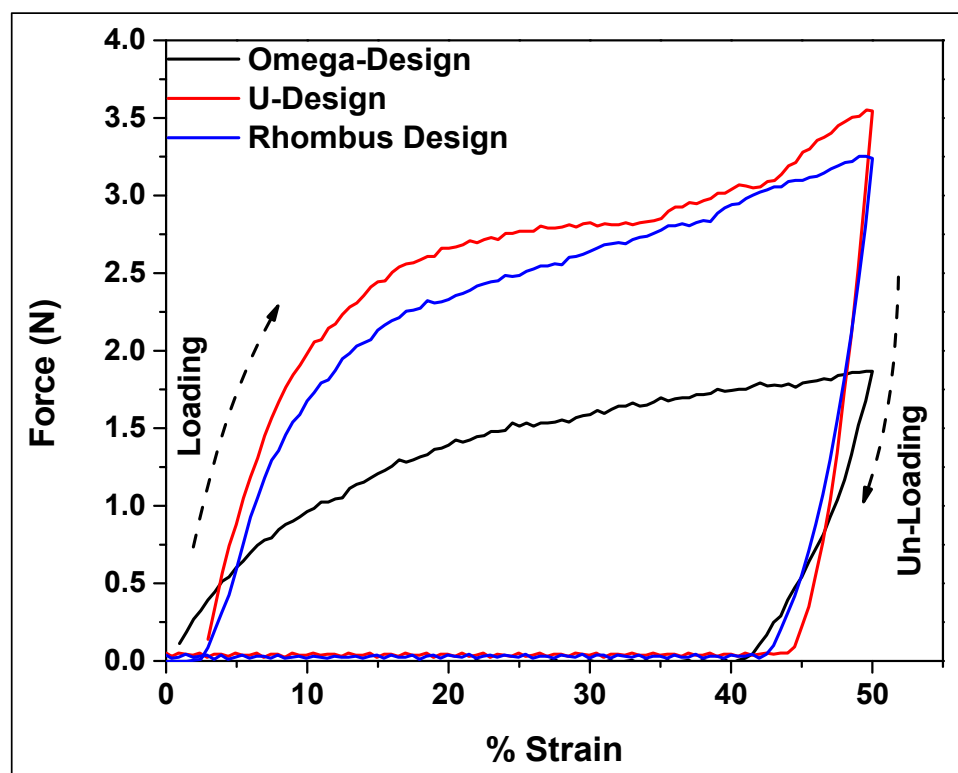


Figure 8. Mechanical behavior of Zn stent with rhombus, U and Omega design under compression after balloon expanding.

Based on this mechanical testing, the rhombus design of the Zn stent showed intermediate values of radial force and percentage strain, which placed it at a “sweet spot” compared to the other two designs. For this reason, rhombus design stents were chosen for Parylene C coating and further analyses.

3.2. Characterization of the Parylene C Coating on Cylindrical Zn Stents

3.2.1. Composition of the Deposited Parylene C Coating

The chemical identity of the Parylene C after depositing a coating on cylindrical, rhombus design Zn stents was characterized by Fourier Transform Infrared Spectroscopy (FTIR). FTIR was conducted within the wavelengths ranging from 4000 to 400cm^{-1} . FTIR analysis illuminates the bonding energy of the Parylene C coating. Figure 9 compares the spectra obtained by FTIR from a) a Parylene C-coated Zn stent, b) a pure Parylene C sample, and c) an uncoated Zn stent. Peaks at $1500\text{--}1600\text{ cm}^{-1}$ represent energy bands of the C=C aromatic stretching. Other peaks at 1050 cm^{-1} and 650 cm^{-1} can be assigned as the bonding energy peaks of chlorobenzene. Peaks at 1450 cm^{-1} are representative of the bonding energies of C=C and CH₂. Finally, peaks at 2860 cm^{-1} and 2923 cm^{-1} indicate bonding energy of the C-H bond in the methyl group and 3000 cm^{-1} designates C-H stretching [28,33,44–46]. From the FTIR study, it was obvious that there was successful formation of a Parylene C polymeric film on the Zn stent.

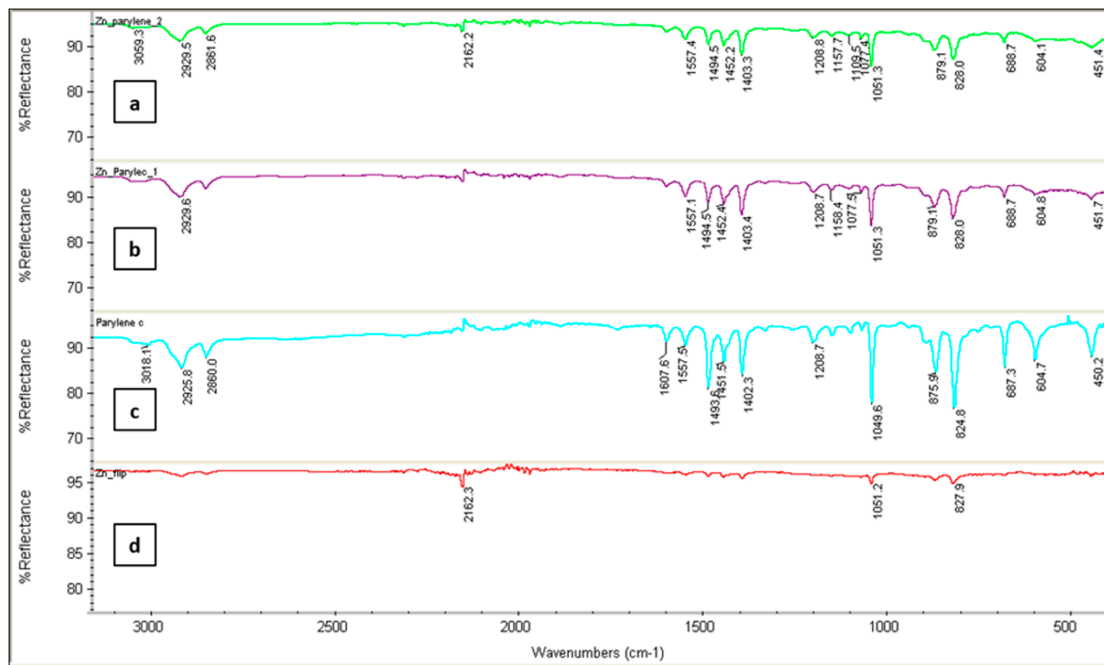


Figure 9. FTIR spectra of: (a) Parylene C-coated Zn stent on random spot 1; (b) Parylene C-coated Zn stent on random spot 2; (c) Pure Parylene C sample; (d) Uncoated Zn stent.

The presence of Parylene C coating on the stent was also evaluated by determining the nature of the carbon bonding in the polymer groups of the Parylene C coating using Raman spectroscopy, analyzing the peaks in the range from 3200 to 160 cm^{-1} . As illustrated in Figure 10a, characteristic peaks at 3100 cm^{-1} represent the aromatic C-H stretching, and the band between 1265–1365 cm^{-1} can be assigned to a CH in-plane deformation [47].

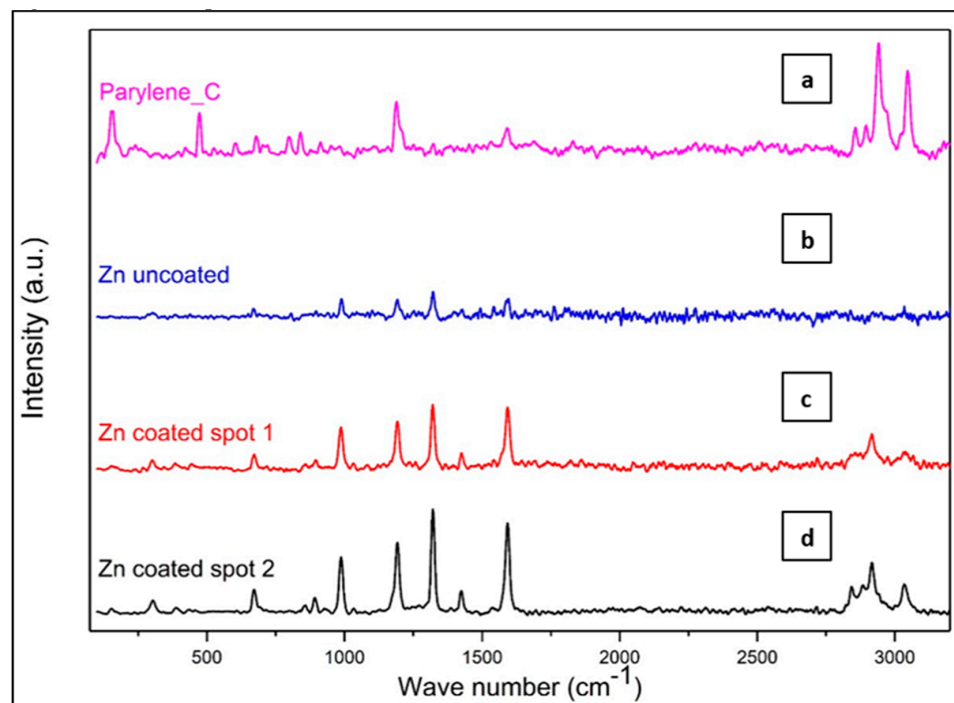


Figure 10. Raman spectroscopy of: (a) Parylene_C Dimer as a control; (b) Uncoated Zn metal; (c) Parylene C-coated stent on random spot 1; (d) Parylene C coated stent on random spot 2.

Figure 10b illustrates the spectrum of the uncoated Zn stent without any prominent peaks. Figure 10c–d displays the spectra of Parylene C coating on Zn stents obtained by probing random spots on the device surface. The peak at 1600 cm^{-1} represents the substitution (para) of chlorine on the benzene rings, while the peaks around $1350\text{--}1500\text{ cm}^{-1}$ can be assigned to CH_2 twisting or C–C skeletal in-plane vibrations of the aromatic ring. The peaks within the range of $750\text{--}1000\text{ cm}^{-1}$ illustrate the out-of-plane deformation of CH [48]. This Raman study further proved that a Parylene C polymeric film was formed on the Zn stent.

3.2.2. Morphology of the Parylene C Coating.

Atomic Force Microscopy (AFM), performing in a tapping mode, was used to evaluate the surface roughness and the phase differences in the polymeric coating on the Zn stents. The polymer coating morphology was further investigated using both secondary and backscattered electrons at a low beam current and voltage of 10 kV. As shown in Figure 11a, the AFM “height image” of the coating suggests relatively even morphology and roughness R_q , R_{qz} and R_{max} of 33.9, 26.8 and 231 nm respectively. The AFM “phase image” in Figure 11b reveals good uniformity of the polymer coating over the surface of the Zn stent.

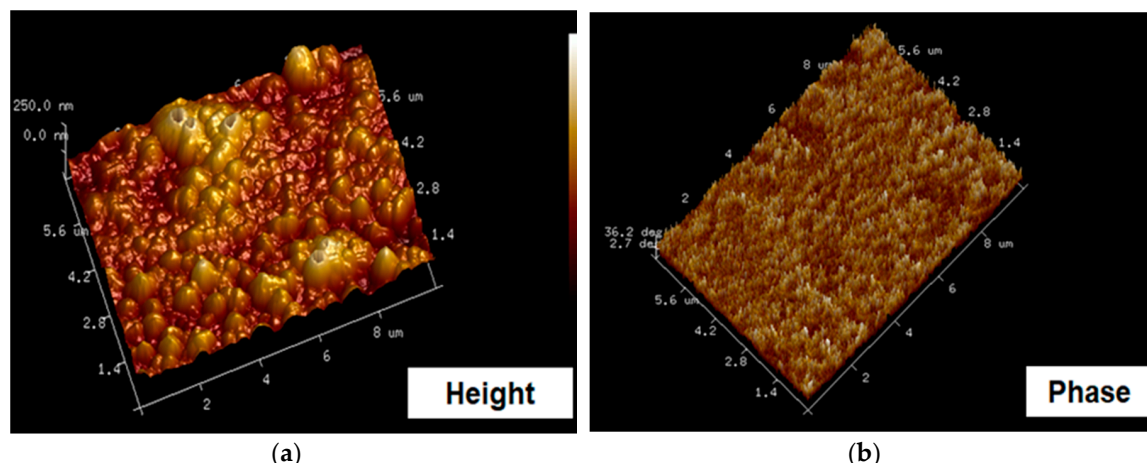


Figure 11. AFM images obtained from the surface of Parylene C-coated Zn stents. (a) Surface morphology of the coating in a “height” mode. (b) Surface image of the polymer in a “phase” mode.

SEM studies of the coating morphology were conducted after the coated stents had been expanded. Conventional stents are usually deployed by dilating at the site of interest in the arteries using a balloon catheter as a delivery system. When such a stent is dilated, it undergoes a mechanical alteration known as elastoplastic deformation. During this process, the polymeric coating on the stent also undergoes mechanical deformation, forming small crevices (openings) on the surface. These crevices provide potential sites for the corrosion process to begin and then propagate after the sample is exposed to a physiological environment. Figure 12 displays both secondary and backscattered electron SEM images from the surface of an expanded, Parylene C-coated Zn stent. Crevices in the coating, which exposed the uncoated Zn metal, were visible with secondary electron imaging (Figure 12a and Figures S2–S4). EDS analyses of stent surfaces are provided in the Supplementary Information, S5–S8), however, the contrast was greatly improved using backscattered electron imaging, as shown in Figure 12b. Figure 12c displays a backscattered electron image of the uniform polymeric coating before stent expansion, obtained in a dark contrast mode where no crevices were observed.

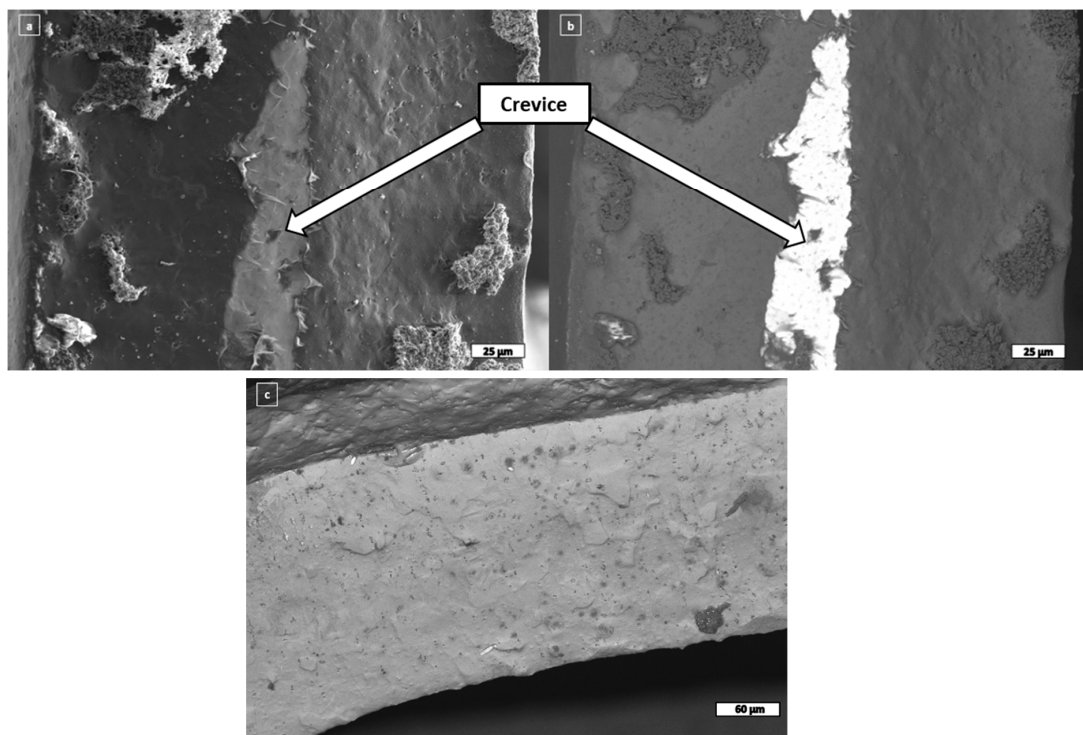


Figure 12. Surface morphology viewed by SEM; (a) Secondary electron image identified crevices in the Parylene C coating on an expanded Zn stent (crevice is lighter gray); (b) Back-scattered electron image (crevice is white); (c) Back-scattered electron image of a strut from an unexpanded stent showing a uniform coating of Parylene C, free of crevices.

3.2.3. Contact Angle Measurements of Uncoated and Parylene C coated Zn Samples.

The hydrophobicity of the tested samples was estimated by conducting contact angle measurements. Initially, a droplet of 1 μL of deionized water was applied to the surfaces. The contact angle on a Parylene C-coated Zn sample was measured and compared with that on an uncoated Zn sample. As displayed in Figure 13a, the contact angle on the Parylene C-coated Zn surface was $\theta = 95.05 \pm 4$ ($n = 5$). This value is close to that reported by M. Kaminska et al. [26], where the contact angle of Parylene C on machined medical steel was 94.25° and on polished medical steel was 92.16° . We believe that there is still room for improvement since the contact angle of an untreated Parylene C film can reach 117° , as demonstrated by J. S. Song et al. [46]. The contact angle on the uncoated Zn sample was $\theta = 84.2 \pm 2$, as shown in Figure 13b. From these measurements, it can be concluded that the Parylene C coating on the Zn surface increased the contact angle and therefore the hydrophobicity of the coated samples. An increase in hydrophobicity can be beneficial for avoiding thrombosis on the stent surface in a physiological environment.

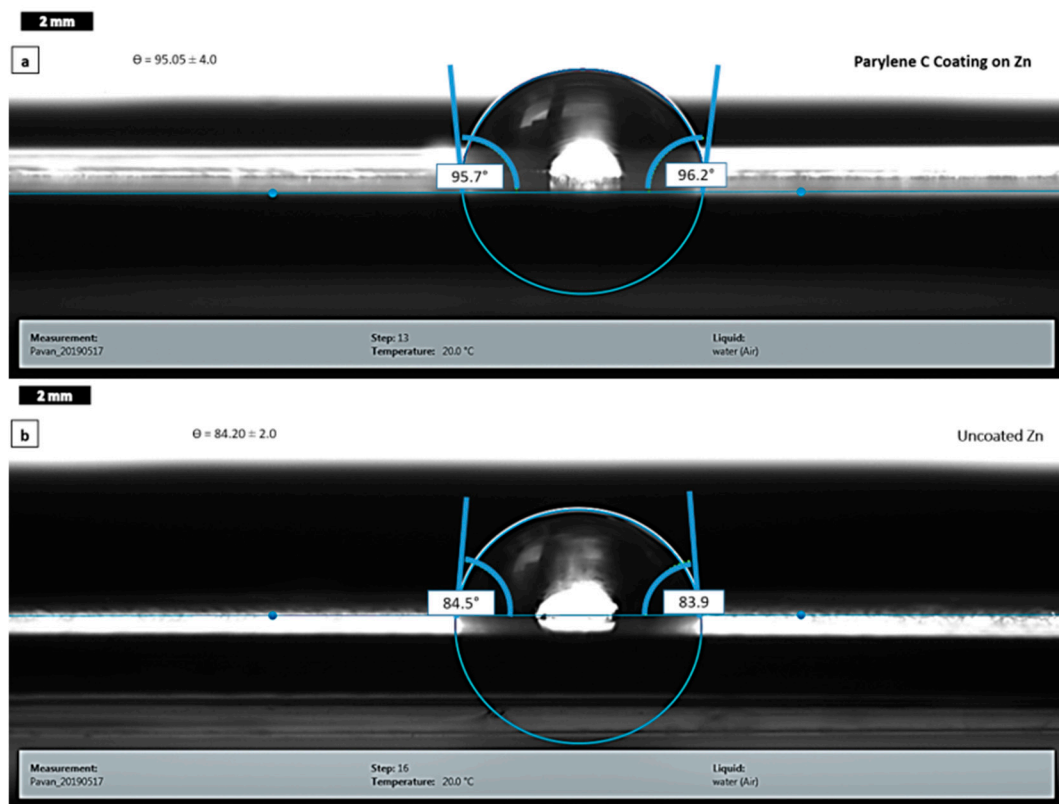


Figure 13. Photographs of water droplets and the measured contact angles Θ on the surface of: (a) Parylene C-coated Zn; (b) Uncoated Zn.

3.3. In-Vitro Study

3.3.1. Corrosion Rate Results Obtained by Weight Loss Measurements

The corrosion rates of the Zn stents were studied by determining the weight loss of the samples after immersion in a standard culture medium containing serum, under cell culture conditions for 72 h, and the results are illustrated in Figure 14. The corrosion rate (rate of degradation) of unexpanded, uncoated Zn stents (assigned here as control samples) was found to be around 0.0951 mm/year, which was lower than that previously observed for Mg and its alloys [13]. Unexpanded Parylene C-coated stents showed a 50% reduction in corrosion rates compared to unexpanded uncoated samples. Expanded stents, both uncoated and coated Zn stents, had a higher corrosion rate than their respective unexpanded stents, presumably because of the elastoplastic deformation caused in the stents by expansion. Expanded Parylene C-coated stents showed a 25% reduction in corrosion rate compared to expanded, uncoated samples. There were significant differences between the conditions, determined by a two-way ANOVA (coating and expansion group p values were each <0.001) and Holm-Sidak post-hoc tests (all conditions differed at the $* p < 0.001$ level, $n = 3$). Parylene C-coated stents degraded at significantly higher rates than uncoated ones, both before and after expansion. Both uncoated and Parylene C-coated samples increased their degradation significantly after expansion. Thus, using this measure of corrosion rate, the rate of corrosion was significantly altered by both coating and expansion. As mentioned earlier, crevices appeared in the polymeric coating during the expansion act and these presumably served as potential corrosion sites by exposing uncoated Zn metal to the culture medium. Thus, the rate of corrosion was significantly altered by both applying coating and conducting expansion.

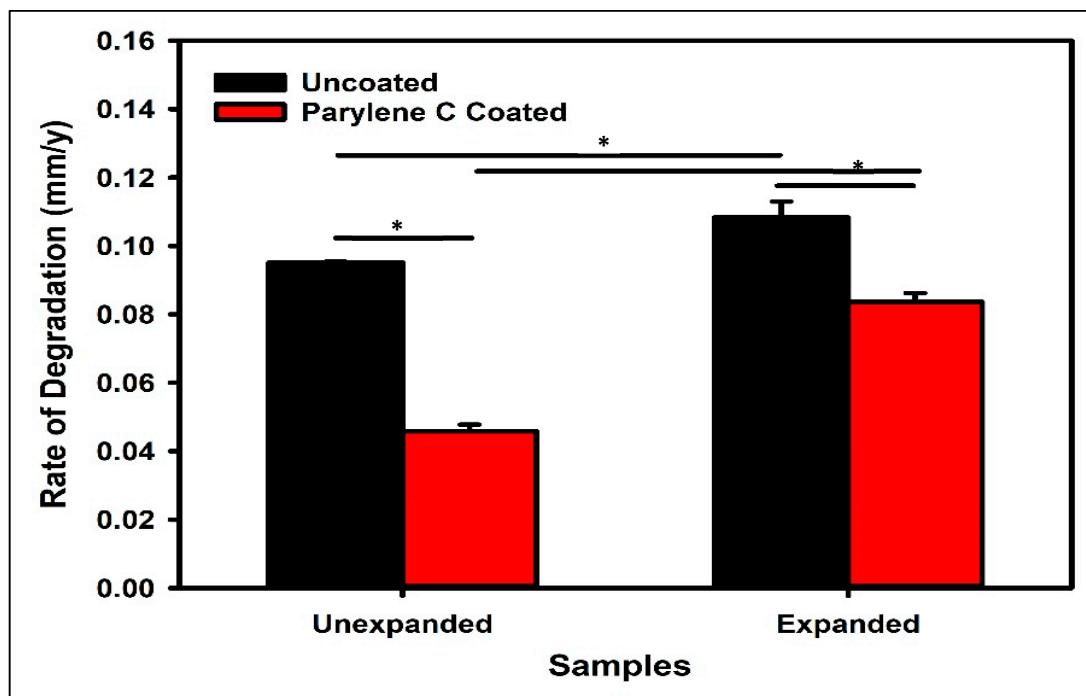


Figure 14. Comparison of corrosion rates between uncoated and Parylene C-coated Zn stent samples before and after expansion. (*) Significance level $p = < 0.001$.

3.3.2. Corrosion Rate Results by ICP-MS

The relative amount of Zn^{2+} (in ppm) released into the culture medium after stent immersion is related to the corrosion rate of the metal. Figure 15 presents a comparison of released Zn^{2+} from uncoated and polymer-coated stents, before and after expansion. The Zn^{2+} concentrations, shown in Figure 15, were significantly affected by the coating (two-way ANOVA, $p = 0.033$ for coating, (n) = 3), but not by expansion ($p = 0.099$). However, when individual comparisons were made using a Holm-Sidak post-hoc multiple comparisons test, there were no differences between the four conditions at the significance level of 0.05. Therefore, the coating made a difference, but only if the expanded and unexpanded samples were considered together. Note that measurements of Zn^{2+} in the medium can be complicated by the fact that Zn^{2+} can be sequestered in precipitates on the metal and therefore would not have been released into the medium, which makes the levels of Zn^{2+} potentially less accurate than the weight measurements. However, the combined effects with both measurements did show that Parylene C coating slowed down the corrosion rate of the devices.

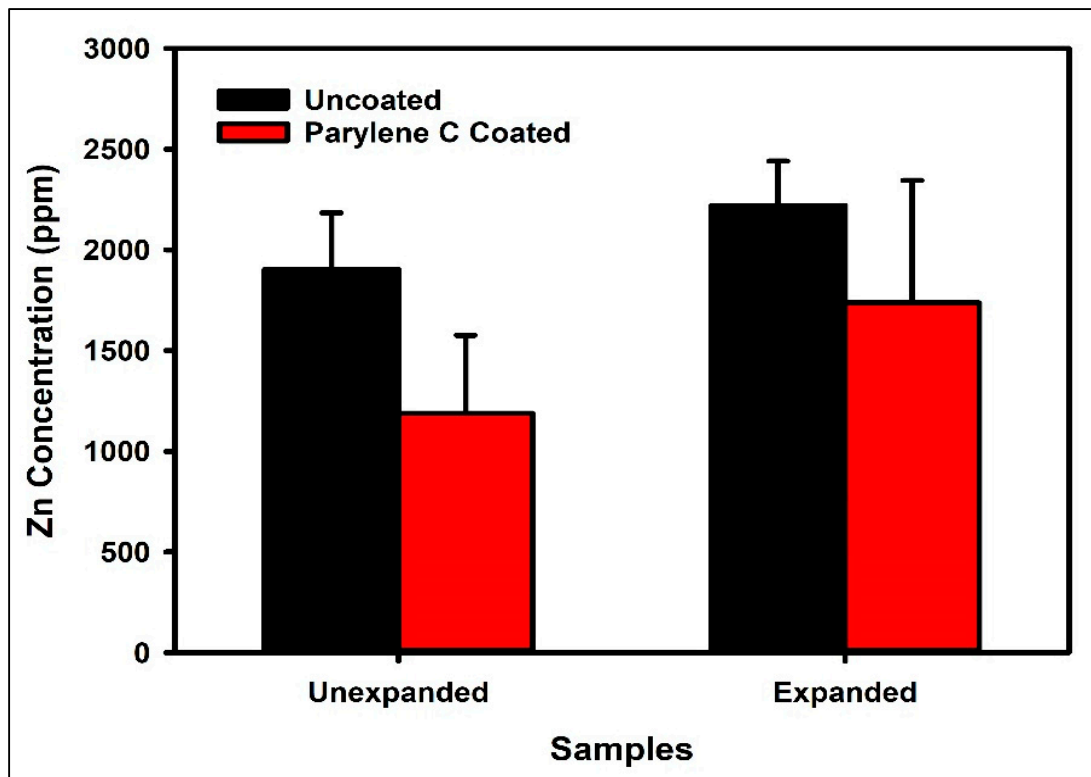


Figure 15. ICP-MS concentration of Zn^{2+} in culture medium after exposure of unexpanded and expanded Zn stent samples, without and with Parylene C coating to the medium for 72 h.

3.4. In Vivo Study

3.4.1. In Vivo Corrosion

Segments of ribbons made of uncoated Zn and AZ31 Mg alloy were implanted under the skin of mice for 15 days. Following euthanasia, the metal segments were removed with the attached skin and observed under an optical microscope. As shown in Figure 16, the Zn ribbon segment was essentially intact (Figure 16a) while the AZ31 Mg segment was more significantly degraded (Figure 16b). Obviously, the corrosion rate of Zn exposed to an in vivo environment was comparatively lower than that of AZ31 Mg.

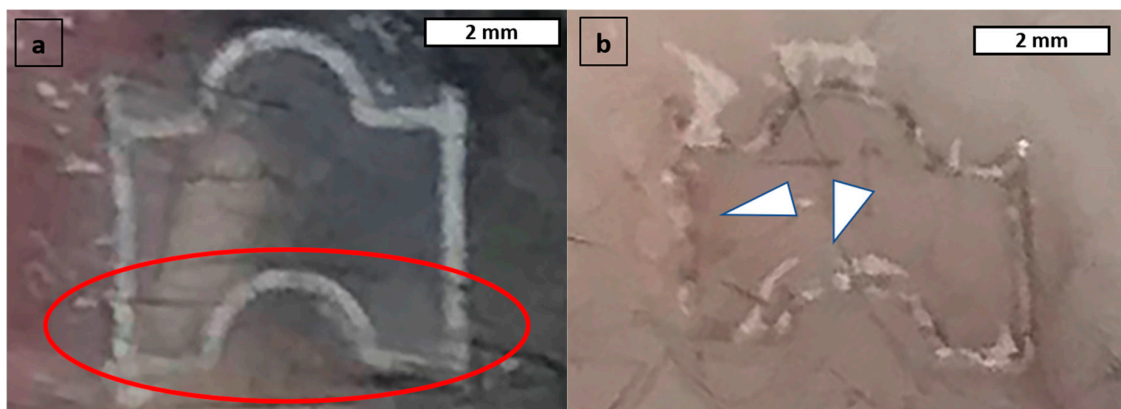


Figure 16. Optical images of ribbon segments after 15 days of subcutaneous implantation: (a) uncoated Zn segment. The red circle shows that the strut outlines were still similar to the original after 15 days; (b) AZ31 Mg alloy segments showed gaps and irregular surfaces (white arrowheads point to a few strikingly corroded areas).

The difference between the degradation of the Zn and AZ31 Mg alloy segments was more pronounced after tissue fixation and tissue clearing using a detergent, as shown in Figure 17. In Figure 17a, the Zn segment can be seen to be quite intact, while in Figure 17b, the AZ31 Mg segment revealed more significant degradation.

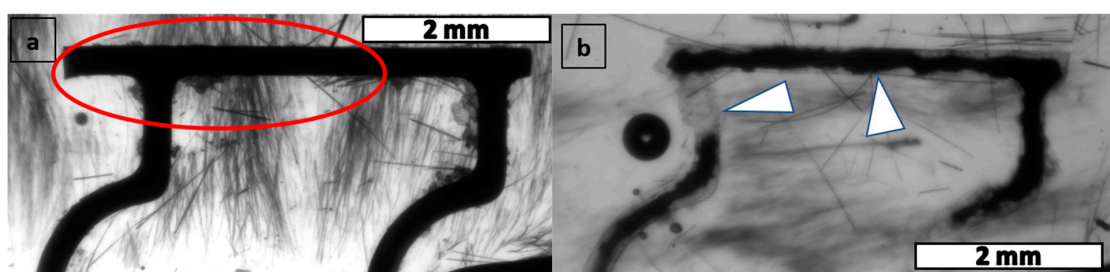


Figure 17. Optical images (taken on a light microscope) of ribbon segments after in vivo implantation for 15 days, removal with skin, tissue fixation, and tissue clearing. (a) An uncoated Zn segment was basically intact. The red circle directs attention to segments of the stents that were intact after 15 days; (b) an AZ31 Mg segment was degraded to a greater extent, as shown by gaps and irregular surfaces (white arrowheads point to a few extensively corroded areas).

3.4.2. Histology study

Half of the explants containing skin and stent samples were embedded in paraffin, sectioned and stained using a standard histological stain (H&E, Figure 18a,b). For both metals, the ribbon material left cavities in the tissue sections because it either degraded during tissue processing (Mg) or, if hard material remained, it almost always rinsed off the sectioned slide. As shown in Figure 18a, the presence of a Mg sample stimulated a very mild inflammatory response, with no significant capsule (black open arrowheads) formation. As shown in Figure 18b, where two sections of Zn segments can be seen, there was slightly more inflammation (black solid arrow points to a region with an accumulation of inflammatory cells). There was a more thickened capsule region around the Zn stent compared to the Mg stent in Figure 18a (black open arrowheads), however, this capsule was still not complex nor dense compared to reactions to other implanted biomaterials. No evidence of necrotic tissue was observed. The thicker capsule with the Zn stent (versus Mg) might be explained by the more intact nature of Zn. A denser material could be somewhat more irritating to the tissues. Other ribbon samples were processed as whole mounts, which were visualized via confocal microscopy (Figure 18c), and paraffin sections were immunostained and viewed via transmission microscopy (Figure 18d,e). In Figure 18c, blood

vessels (non-specifically labeled in this view due to the autofluorescence of red blood cells) appeared as light green (arrows). The blood vessels clustered closely around the stent material. This suggests that the Zn ribbon was not irritating to the vessels and there was no dense capsule that prevented blood vessels from approaching the metal. Sections from the paraffin-embedded stents were also immunostained for the presence of axons (with an antibody against a neurofilament protein, red in Figure 18d,e) and blood vessels (with an antibody against smooth muscle actin, green in Figure 18d,e). Figure 18d and e show the immunostaining of sections from a Mg (Figure 18d) and Zn (Figure 18e) explant. In both, nerves (open white arrows) and blood vessels (solid white arrows) were seen in tissues close to the explant (outline of explant is shown in white). Nuclei are labeled blue in 18d and e. Taken together, the histological staining suggested no toxicity of either ribbon material and excellent biocompatibility with normal tissues.

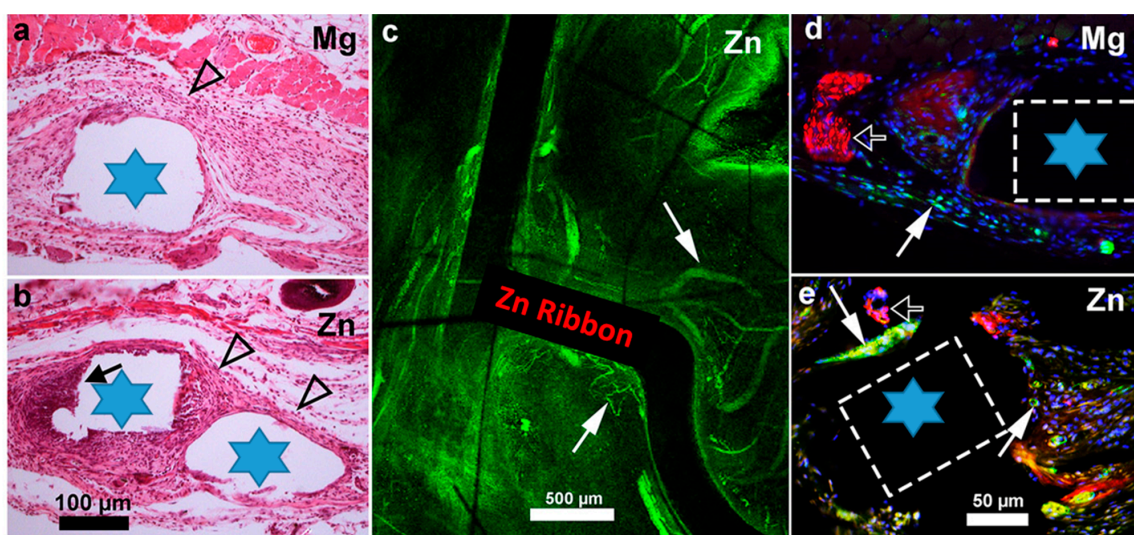


Figure 18. Histology of Mg and Zn ribbon pieces after in vivo implantation: (a,b) sections stained with H&E; (c) whole mount immunofluorescence; and (d,e) sections immunostained for axons (red), blood vessels (green) and nuclei (blue). Little to no capsule (a,b, open arrowheads) formed around the cavities which had contained ribbon pieces (stars) and there was little inflammation (black arrow, b). Blood vessels clustered extensively around the stents (c–e, white arrows). Immunostaining confirmed that (d,e) both blood vessels (solid white arrows) and nerves (open arrows) were found close to the ribbon pieces (location indicated by white rectangles). (Bar in b applies to a and bar in e applies to d).

4. Conclusions

This study demonstrated that photo-chemical etching is a robust approach for the fabrication of biodegradable Zn stents. Cylindrical Zn stents with different patterns were made using this method and successfully tested for balloon expansion and mechanical compression. The stents with a rhombus design expanded smoothly and uniformly, both with and without a Parylene C coating. A Parylene C coating on the Zn stents served as a moderate corrosion barrier in vitro, thus slowing down the device degradation when exposed to a standard culture medium with serum. After in vivo implantation, segments of Zn ribbon samples showed a significantly slower rate of degradation than Mg ribbon samples. The Zn segments were also seen to be non-toxic to surrounding tissues, stimulating only a mild inflammatory response, and showed excellent compatibility with nerves and blood vessels. Tissue reactions to segments of the Zn ribbon were comparable to the reactions to AZ31 Mg samples. Therefore, both in vitro and in vivo studies conducted with pure Zn metal stent materials, made by photo-chemical etching, confirmed that Zn is a promising material for biodegradable stent applications.

Supplementary Materials: The following are available online at <http://www.mdpi.com/2076-3417/9/21/4503/s1>, Table S1: General criteria applied to biodegradable materials for use in stent applications [1]. Reproduced from [1] with permission from John Wiley and Sons; Figure S1: Radiopacity of three Zn stents, made via photo-chemical etching, after exposure to X-ray; Figure S2: SEM images of unexpanded Zn stents, after immersion corrosion, but before removal of surface corrosion deposits. (a) Significant corrosion is seen with a bare Zn stent; (b) Polymeric folds are observed on the surface of a Parylene C coated Zn stent; Figure S3: (a) Surface morphology revealed by SEM of an unexpanded, uncoated Zn stent after cleaning, at 2000x. (b) Surface morphology of the same stent at 5000x. The arrow shows the area in a that is shown in b; Figure S4: (a) Surface morphology of a Parylene C coated Zn stent after expansion, corrosion for 72 h in the culture medium, and removal of the degradation products, showing crevices in the polymeric film when imaged by SEM in a secondary electron mode; (b) The crevices are even better visualized when using SEM in a back-scattered electron mode (same location as in Figure S4a); (c) Surface morphology of an unexpanded Parylene C coated Zn stent after corrosion and cleaning, shows relatively smaller crevices in the polymeric film when imaged by SEM in a back-scattered electron mode; Figure S5: (a) SEM image of two selected areas on an uncoated stent with corrosion products before cleaning; (b) EDS analysis of selected area 1; (c) EDS analysis of selected area 2; Figure S6: SEM image of a Parylene C coated Zn stent with corrosion products on its surface, before cleaning; (a) EDS analysis of selected area 1; (b) EDS analysis of selected area_2; Figure S7: (a) SEM image of an uncoated stent after cleaning; (b) EDS analysis selected area 1; Figure S8: (a) SEM of a Parylene C coated and expanded stent with corrosion products, after cleaning; (b) EDS analysis of selected area 1; (c) EDS analysis of selected area 2.

Author Contributions: B.S.P.K.K., G.Z. and V.S. created the Zn stents by photo-chemical etching and tested their mechanical behavior, coated the stents with Parylene C and performed in vitro corrosion experiments. B.S.P.K.K., contributed the most to characterization of stents and was responsible for the initial draft of the manuscript. T.M.H., X.A., and S.K.P. performed the in vivo experiments and subsequent tissue processing and assisted with manuscript writing.

Funding: The authors would like to acknowledge the financial support provided by the NSF ERC for Revolutionizing Biomaterials through grant EEC-EEC-0812348.

Acknowledgments: We wish to thank Mark Paquin for the help with the stent compression test and the Cincinnati Children's Hospital Medical Center (CCHMC) for assistance with imaging and sample preparation.

Conflicts of Interest: The authors declare no conflict of interest.

References

1. Finegold, J.A.; Asaria, P.; Francis, D.P. Mortality from ischaemic heart disease by country, region, and age: Statistics from World Health Organisation and United Nations. *Int. J. Cardiol.* **2013**, *168*, 934–945. [[CrossRef](#)]
2. Kastrati, A.; Mehilli, J.; Dirschinger, J.; Pache, J.; Ulm, K.; Schühlen, H.; Seyfarth, M.; Schmitt, C.; Blasini, R.; Neumann, F.J.; et al. Restenosis after coronary placement of various stent types. *Am. J. Cardiol.* **2001**, *87*, 34–39. [[CrossRef](#)]
3. Bowen, P.K.; Drelich, J.; Goldman, J. Zinc exhibits ideal physiological corrosion behavior for bioabsorbable stents. *Adv. Mater.* **2013**, *25*, 2577–2582. [[CrossRef](#)]
4. Katarivas Levy, G.; Goldman, J.; Aghion, E. The Prospects of Zinc as a Structural Material for Biodegradable Implants—A Review Paper. *Metals* **2017**, *7*, 402. [[CrossRef](#)]
5. Bowen, P.K.; Shearier, E.R.; Zhao, S.; Guillory, R.J.; Zhao, F.; Goldman, J.; Drelich, J.W. Biodegradable Metals for Cardiovascular Stents: From Clinical Concerns to Recent Zn-Alloys. *Adv. Healthc. Mater.* **2016**, *5*, 1121–1140. [[CrossRef](#)]
6. Zhao, Z.X.; Hua, Z.M.; Li, D.W.; Wei, D.S.; Liu, Y.; Wang, J.G.; Luo, D.; Wang, H.Y. Effect of Sn content on the microstructure, mechanical properties and corrosion behavior of biodegradable Mg-x (1, 3 and 5 wt.%) Sn-1Zn-0.5Ca alloys. *Materials* **2018**, *11*, 2378. [[CrossRef](#)]
7. Niu, J.; Tang, Z.; Huang, H.; Pei, J.; Zhang, H.; Yuan, G.; Ding, W. Research on a Zn-Cu alloy as a biodegradable material for potential vascular stents application. *Mater. Sci. Eng. C* **2016**, *69*, 407–413. [[CrossRef](#)]
8. Han, P.; Tan, M.; Zhang, S.; Ji, W.; Li, J.; Zhang, X.; Zhao, C.; Zheng, Y.; Chai, Y. Shape and site dependent in vivo degradation of Mg-Zn pins in rabbit femoral condyle. *Int. J. Mol. Sci.* **2014**, *15*, 2959–2970. [[CrossRef](#)]
9. Yang, H.; Wang, C.; Liu, C.; Chen, H.; Wu, Y.; Han, J.; Jia, Z.; Lin, W.; Zhang, D.; Li, W.; et al. Evolution of the degradation mechanism of pure zinc stent in the one-year study of rabbit abdominal aorta model. *Biomaterials* **2017**, *145*, 92–105. [[CrossRef](#)]
10. Jackson, M.J. *Physiology of Zinc: General Aspects; Zinc in Human Biology*; Springer: London, UK, 1989; pp. 1–14.
11. Plum, L.M.; Rink, L.; Hajo, H. The essential toxin: Impact of zinc on human health. *Int. J. Environ. Res. Public Health* **2010**, *7*, 1342–1365. [[CrossRef](#)]

12. Tapiero, H.; Tew, K.D. Trace elements in human physiology and pathology: Zinc and metallothioneins. *Biomed. Pharmacother.* **2003**, *57*, 399–411. [[CrossRef](#)]
13. Koo, Y.; Tiasha, T.; Shanov, V.N.; Yun, Y. Expandable Mg-based Helical Stent Assessment using Static, Dynamic, and Porcine Ex Vivo Models. *Sci. Rep.* **2017**, *7*, 1–10. [[CrossRef](#)]
14. Shanov, V.N.; Roy-Chaudhury, P.; Schulz, M.; Yin, Z.; Campos-Naciff, B.; Wang, Y. Making Magnesium Biodegradable Stent for Medical Implant Applications. U.S. Patent 9,655,752, 23 May 2017.
15. Ye, S.H.; Chen, Y.; Mao, Z.; Gu, X.; Shankararaman, V.; Hong, Y.; Shanov, V.; Wagner, W.R. Biodegradable Zwitterionic Polymer Coatings for Magnesium Alloy Stents. *Langmuir* **2019**, *35*, 1421–1429. [[CrossRef](#)]
16. Coyan, G.N.; D’Amore, A.; Matsumura, Y.; Pedersen, D.D.; Luketich, S.K.; Shanov, V.; Katz, W.E.; David, T.E.; Wagner, W.R.; Badhwar, V. In vivo functional assessment of a novel degradable metal and elastomeric scaffold-based tissue engineered heart valve. *J. Thorac. Cardiovasc. Surg.* **2019**, *157*, 1809–1816. [[CrossRef](#)]
17. Chen, Y.; Ye, S.H.; Sato, H.; Zhu, Y.; Shanov, V.; Tiasha, T.; D’Amore, A.; Luketich, S.; Wan, G.; Wagner, W.R. Hybrid scaffolds of Mg alloy mesh reinforced polymer/extracellular matrix composite for critical-sized calvarial defect reconstruction. *J. Tissue Eng. Regen. Med.* **2018**, *12*, 1374–1388. [[CrossRef](#)]
18. Wang, J.; Giridharan, V.; Shanov, V.; Xu, Z.; Collins, B.; White, L.; Jang, Y.; Sankar, J.; Huang, N.; Yun, Y. Flow-induced corrosion behavior of absorbable magnesium-based stents. *Acta Biomater.* **2014**, *10*, 5213–5223. [[CrossRef](#)]
19. Gu, X.; Mao, Z.; Ye, S.-H.; Koo, Y.; Yun, Y.; Tiasha, T.R.; Shanov, V.; Wagner, W.R. Biodegradable, elastomeric coatings with controlled anti-proliferative agent release for magnesium-based cardiovascular stents. *Coll. Surf. B. Biointerfaces* **2016**, *144*, 170–179. [[CrossRef](#)]
20. Mostaed, E.; Sikora-Jasinska, M.; Drelich, J.W.; Vedani, M. Zinc-based alloys for degradable vascular stent applications. *Acta Biomater.* **2018**, *71*, 1–23. [[CrossRef](#)]
21. Drelich, A.J.; Zhao, S.; Guillory, R.J.; Drelich, J.W.; Goldman, J. Long-term surveillance of zinc implant in murine artery: Surprisingly steady biocorrosion rate. *Acta Biomater.* **2017**, *58*, 539–549. [[CrossRef](#)]
22. Guillory, R.J.; Bowen, P.K.; Hopkins, S.P.; Shearier, E.R.; Earley, E.J.; Gillette, A.A.; Aghion, E.; Bocks, M.; Drelich, J.W.; Goldman, J. Corrosion Characteristics Dictate the Long-Term Inflammatory Profile of Degradable Zinc Arterial Implants. *ACS Biomater. Sci. Eng.* **2016**, *2*, 2355–2364. [[CrossRef](#)]
23. Vojtech, D.; Kubasek, J.; Serak, J.; Novak, P. Mechanical and corrosion properties of newly developed biodegradable Zn-based alloys for bone fixation. *Acta Biomater.* **2011**, *7*, 3515–3522. [[CrossRef](#)]
24. Jablonska, E.; Vojtech, D.; Fousova, M.; Kubasek, J.; Lipov, J.; Fojt, J.; Rumel, T. Influence of surface pre-treatment on the cytocompatibility of a novel biodegradable ZnMg alloy. *Mater. Sci. Eng. C* **2016**, *68*, 198–204. [[CrossRef](#)]
25. Li, H.F.; Xie, X.H.; Zheng, Y.F.; Cong, Y.; Zhou, F.Y.; Qiu, K.J.; Wang, X.; Chen, S.H.; Huang, L.; Tian, L.; et al. Development of biodegradable Zn-1X binary alloys with nutrient alloying elements Mg, Ca and Sr. *Sci. Rep.* **2015**, *5*, 1–14.
26. Kaminska, M.; Okroj, W.; Szymanski, W.; Jakubowski, W.; Komorowski, P.; Nosal, A.; Szymanowski, H.; Gazicki-Lipman, M.; Jerczynska, H.; Pawłowska, Z.; et al. Interaction of parylene C with biological objects. *Acta Bioeng. Biomech.* **2009**, *11*, 19–25.
27. Fontaine, A.B.; Koelling, K.; Dos Passos, S.; Cearlock, J.; Hoffman, R.; Spigos, D.G. Polymeric Surface Modifications of Tantalum Stents. *J. Endovasc. Surg.* **2004**, *3*, 276–283. [[CrossRef](#)]
28. Surmeneva, M.A.; Vladescu, A.; Cotrut, C.M.; Tyurin, A.I.; Pirozhkova, T.S.; Shuvarin, I.A.; Elkin, B.; Oehr, C.; Surmenev, R.A. Effect of parylene C coating on the antibiocorrosive and mechanical properties of different magnesium alloys. *Appl. Surf. Sci.* **2018**, *427*, 617–627. [[CrossRef](#)]
29. Kandala, B.S.P.K.; Zhang, G.; LCorriveau, C.; Paquin, M.; Shanov, V. In Vivo Study of Magnesium AZ31 Stent Fabricated by Photo-Chemical Etching. manuscript in progress.
30. Frazin, L.J.; Lanza, G.; Vonesh, M.; Khasho, F.; Spizzzeri, C.; McGee, S.; Mehlman, D.; Chandran, K.B.; Talano, J.; McPherson, D. Functional chiral asymmetry in descending thoracic aorta. *Circulation* **1990**, *82*, 1985–1994. [[CrossRef](#)]
31. Segadal, L.; Matre, K. Blood velocity distribution in the human ascending aorta. *Circulation* **1987**, *76*, 90–100. [[CrossRef](#)]
32. Karino, T.; Goldsmith, H.L.; Motomiya, M.; Mabuchi, S.; Sohara, Y. Flow patterns in vessels of simple and complex geometries. In *Blood in Contact with Natural and Artificial Surfaces*; Leonard, E.F., Turitto, V.T., Vroman, L., Eds.; Academy Press: New York, NY, USA, 1987; pp. 422–441.

33. Kahouli, A.; Sylvestre, A.; Ortega, L.; Jomni, F.; Yangui, B.; Maillard, M.; Berge, B.; Robert, J.C.; Legrand, J. Structural and dielectric study of parylene C thin films. *Appl. Phys. Lett.* **2009**, *94*. [[CrossRef](#)]
34. Cieslik, M.; Engvall, K.; Pan, J.; Kotarba, A. Silane-parylene coating for improving corrosion resistance of stainless steel 316 L implant material. *Corros. Sci.* **2011**, *53*, 296–301. [[CrossRef](#)]
35. Spiro, R.G. Studies on Fetuin, a Glycoprotein of Fetal Serum. *J. Biol. Chem.* **1960**, *235*, 2860–2869.
36. International Standard ISO 8407 ISO 10993-12; ISO: Geneva, Switzerland, 2009.
37. Liu, L.; Meng, Y.; Dong, C.; Yan, Y.; Volinsky, A.A.; Wang, L.N. Initial formation of corrosion products on pure zinc in simulated body fluid. *J. Mater. Sci. Technol.* **2018**, *34*, 2271–2282. [[CrossRef](#)]
38. ASTM Standard Practice for Laboratory Immersion Corrosion Testing of Metals. In *Annual Book of ASTM Standards*; ASM International Philadelphia: Philadelphia, PA, USA.
39. Ibrahim, H.; Klärner, A.D.; Poorganji, B.; Dean, D.; Luo, A.A.; Elahinia, M. Microstructural, mechanical and corrosion characteristics of heat-treated Mg-1.2Zn-0.5Ca (wt%) alloy for use as resorbable bone fixation material. *J. Mech. Behav. Biomed. Mater.* **2017**, *69*, 203–212. [[CrossRef](#)]
40. Vennemeyer, J.; Hopkins, T.; Hershcovitch, M.; Little, K.; Hagen, M.; Minteer, D.; Hom, D.; Marra, K.; Pixley, S. Initial observations on using magnesium metal in peripheral nerve repair. *J. Biomater. Appl.* **2015**, *344*, 1145–1154. [[CrossRef](#)]
41. Asgari, M.; Hang, R.; Wang, C.; Yu, Z.; Li, Z.; Xiao, Y. Biodegradable Metallic Wires in Dental and Orthopedic Applications: A Review. *Metals* **2018**, *8*, 212. [[CrossRef](#)]
42. Dent, J.A.; Polson, A.G.; Klymkowsky, M.W. A whole-mount immunocytochemical analysis of the expression of the intermediate filament protein vimentin in *Xenopus*. *Development* **1989**, *105*, 61–74.
43. Rieu, R.; Barragan, P.; Masson, C.; Fuseri, J.; Garitey, V.; Silvestri, M.; Roquebert, P. Radial force of coronary stents: A comparative analysis. *Catheter. Cardiovasc. Interv.* **1999**, *46*, 380–391. [[CrossRef](#)]
44. Lee, T.; Lee, J.; Park, C. Characterization of parylene deposition process for the passivation of organic light emitting diodes. *Korean J. Chem. Eng.* **2002**, *19*, 722–727. [[CrossRef](#)]
45. Bera, M.; Rivaton, A.; Gandon, C.; Gardette, J.L. Comparison of the photodegradation of parylene C and parylene N. *Eur. Polym. J.* **2000**, *36*, 1765–1777. [[CrossRef](#)]
46. Song, J.S.; Lee, S.; Jung, S.H.; Cha, G.C.; Mun, M.S. Improved Biocompatibility of Parylene-C Films Prepared by Chemical Vapor Deposition and the Subsequent Plasma Treatment. *J. Appl. Polym. Sci.* **2010**, *116*, 2658–2667. [[CrossRef](#)]
47. Balss, K.M.; Llanos, G.; Papandreou, G.; Maryanoff, C.A. Quantitative spatial distribution of sirolimus and polymers in drug-eluting stents using confocal Raman microscopy. *J. Biomed. Mater. Res. Part A* **2008**, *85*, 258–270. [[CrossRef](#)]
48. Mathur, M.S.; Weir, A. Laser Raman and Infrared Spectrum of Poly-p-Xylylene. *J. Mol. Struct.* **1973**, *15*, 459–463. [[CrossRef](#)]



© 2019 by the authors. Licensee MDPI, Basel, Switzerland. This article is an open access article distributed under the terms and conditions of the Creative Commons Attribution (CC BY) license (<http://creativecommons.org/licenses/by/4.0/>).